

Reliable Face Morphing Attack Detection in On-The-Fly Border Control Scenario with Variation in Image Resolution and Capture Distance

Jag Mohan Singh Raghavendra Ramachandra

Norwegian University of Science and Technology (NTNU), Gjøvik

E-mail: {jag.m.singh, raghavendra.ramachandra} @ ntnu.no

Abstract

Face Recognition Systems (FRS) are vulnerable to various attacks performed directly and indirectly. Among these attacks, face morphing attacks are highly potential in deceiving automatic FRS and human observers and indicate a severe security threat, especially in the border control scenario. This work presents a face morphing attack detection, especially in the On-The-Fly (OTF) Automatic Border Control (ABC) scenario. We present a novel Differential-MAD (D-MAD) algorithm based on the spherical interpolation and hierarchical fusion of deep features computed from six different pre-trained deep Convolutional Neural Networks (CNNs). Extensive experiments are carried out on the newly generated face morphing dataset (SCFace-Morph) based on the publicly available SCFace dataset by considering the real-life scenario of Automatic Border Control (ABC) gates. Experimental protocols are designed to benchmark the proposed and state-of-the-art (SOTA) D-MAD techniques for different camera resolutions and capture distances. Obtained results have indicated the superior performance of the proposed D-MAD method compared to the existing methods.

1. Introduction

Face biometrics are widely deployed in various high-security applications, including border control, by considering usability, high accuracy, and non-intrusive capture. The high accuracy of the face biometrics can be attributed to the advances in deep-learning-based FRS methods [16, 17, 18]. The exponential growth in face recognition applications has also increased the vulnerability to various attacks. Among different types of attacks on the Face Recognition Systems (FRS), the morphing attacks have mainly gained much interest due to their vulnerability in the border control scenario. The morphing process will perform the blending operation on the given face images (from contributory data subjects) to generate a single Face Morphing Image (FMI).

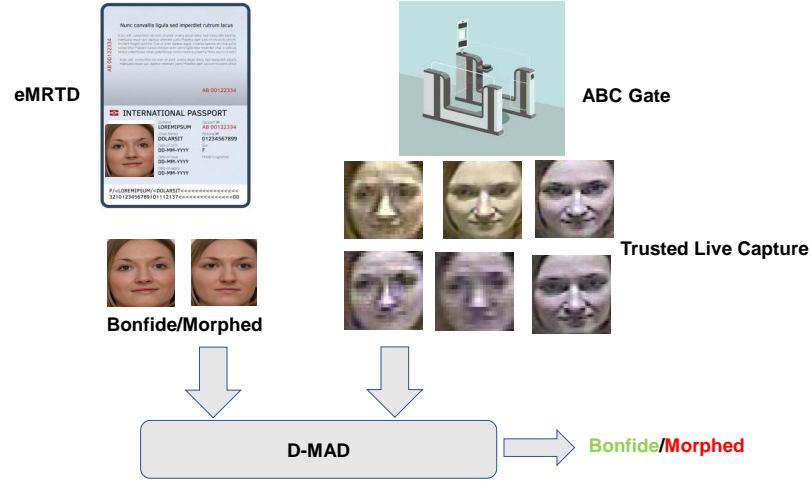


Figure 1. Illustration showing eMRTD presentation at an ABC Gate and D-MAD based decision.

Thus, the generated FMI includes the facial properties from all the contributory data subjects, thus demonstrating the vulnerability of both automatic FRS and human observers [19]. Since the morphing face images could be used to obtain the electronic Machine Readable Travel Document (eMRTD) or e-passports, the malicious person can exploit this process to cross the border through Automated Border Control (ABC) gates.

Face Morph Attack Detection (MAD) algorithms are extensively addressed in the biometric literature [20]. Available MAD algorithms can be classified into two main categories [20] (a) Single image based-MAD (S-MAD), where morph attacks are detected based on a single image (b) Differential MAD (D-MAD) algorithms, where morphing attacks are detected based on two or more images. Among these two approaches, the D-MAD-based MAD techniques have attracted biometric researchers by considering their application in the border control scenario. Figure 1 illustrates the D-MAD scenario in the border control application. The early work on the D-MAD approach is based on

Algorithm	Algorithm Classification	Brief Description
Landmark [1]	Landmark Based	Directed Landmark shifts used for classification
Feature-based [2]	Feature difference based	Feature Difference used for classification
Fusion of classifiers based [3]	Fusion of classifiers	Fusion of hand-crafted (LBPH) and CNN-based (TDCNN) features
FD-GAN [4]	FD-GAN	Image Demorphing using symmetric dual GAN
LRP [5]	LRP	Layer-Wise Relevance Propagation based on pixel-wise decision
Siamese [6]	Siamese Architecture	Siamese Architecture based on Inception ResNET v1 with weights from VGGFace2
Mutual Information Maximization [7]	Disentanglement	Disentanglement of Appearance and Landmarks based on CNN
Demorphing [8]	Image Subtraction	Inverting Morphing Equation with image-pair and known correspondences and α
Fusion of CNN features [9]	Fusion of Classifiers	Shape (Normal-Map) and Reflectance (Diffuse Reconstruction) Decomposition: SfS-Net and Alexnet
DFR [10]	DFR	Signed Distance of Arcface and Facenet features
Demorphing [11]	Demorphing	Autoencoder-based demorphing and face similarity analysis
Siamese [12]	Siamese	Siamese for D-MAD trained on wavelet basis chosen using Kullback-Liebler Divergence (KLD)
Double Siamese [13]	Double Siamese	Double-Siamese based D-MAD, identity-based and artifact-based
GAN [14]	GAN	Conditional Identity Disentanglement using Conditional GAN for D-MAD
Legacy [15]	Legacy	Legacy Image and Face Verification Engine score based D-MAD

Table 1. State-of-the-art D-MAD techniques

the face demorphing [8], followed by several existing methods summarised in Table 1. The D-MAD approaches are developed using conventional hand-crafted features and deep features derived from pre-trained CNNs based on natural and face images [20].

The deep learning approaches based on GAN, Siamese and Double Siamese have also been proposed for D-MAD. The benchmarking of existing D-MAD techniques is discussed in [20, 21] on the data captured using ABC gates indicate the severity of the problem by showing the degraded results. The ABC gate scenarios used in [21] are based on the one-stop such that the data subject will stand still in front of the ABC gate camera. Thus, this scenario will generate constrained images less prone to the pose and environmental (external lighting) conditions. In [9], the ABC scenario based on the 'on-the-fly' face capture and 3D information-based D-MAD method was introduced. Since 'on-the-fly' (OTF) face capture will result in variations in face pose, expression, and lighting, the D-MAD techniques based on face demorphing and conventional features have indicated the degraded performance [9]. The experimental results with different lighting conditions indicate the further degradation of the 3D-based D-MAD results. However, it is essential to note that the existing D-MAD literature did not consider the option of different cameras with varying capture resolution and capture distance impacting the detection performance. Since the D-MAD techniques are expected to work with different ABC gates with varying camera resolutions, it is necessary to devise a suitable D-MAD method for this scenario. Thus, we are motivated to consider the OTF ABC gate scenario with various camera resolutions and different capture distances in this work.

This work proposes a novel algorithm for a robust D-MAD, especially in the OTF ABC Gate scenario with varying image resolutions and capture distances. To this extent, we introduce a novel D-MAD algorithm based on spherical interpolation and the hierarchical fusion of deep features to detect morphing attacks. The deep features are extracted using six different pre-trained deep CNN networks that are

combined using a hierarchical fusion at both the score level and feature level. Extensive experiments are carried out on the newly created database SCFace-Morph using the publicly available SCFace [22] database with 130 data subjects captured using both controlled and uncontrolled scenarios with different resolution cameras and different capture distances. We construct the new face morphing dataset SCFace-Morph dataset using landmark-based face morphing tools [23] and re-digitize (or print-scan) the face morphing images to represent the real-life scenario of the border control.

The following are the main contributions of our work:

- Proposed a novel D-MAD algorithm based on spherical interpolation and hierarchical fusion of deep features for reliable face morphing attack detection.
- Introduced a new face morphing dataset (SCFace-Morph) constructed using the publicly available dataset (SCFace [22]) for both digital and Print-Scan (PS) morphing attacks. *To the best of our knowledge, this is the first work exploring morphing attack detection on the different camera resolutions and at various capture distances suitable for the OTF ABC scenario.*
- Extensive experiments are carried out to benchmark the performance of the proposed method with the SOTA techniques.

The rest of the paper is organized as follows: we present the proposed method in Section 2, experiments and results are discussed in Section 3 and finally conclusions and future work is discussed in Section 4.

2. Proposed Method

Figure 2 shows the block diagram of the proposed method for robust D-MAD, especially in the OTF border control scenario. The proposed method is designed effectively to capture the variation of the face quality in terms of environmental changes due to lighting, pose, and expression

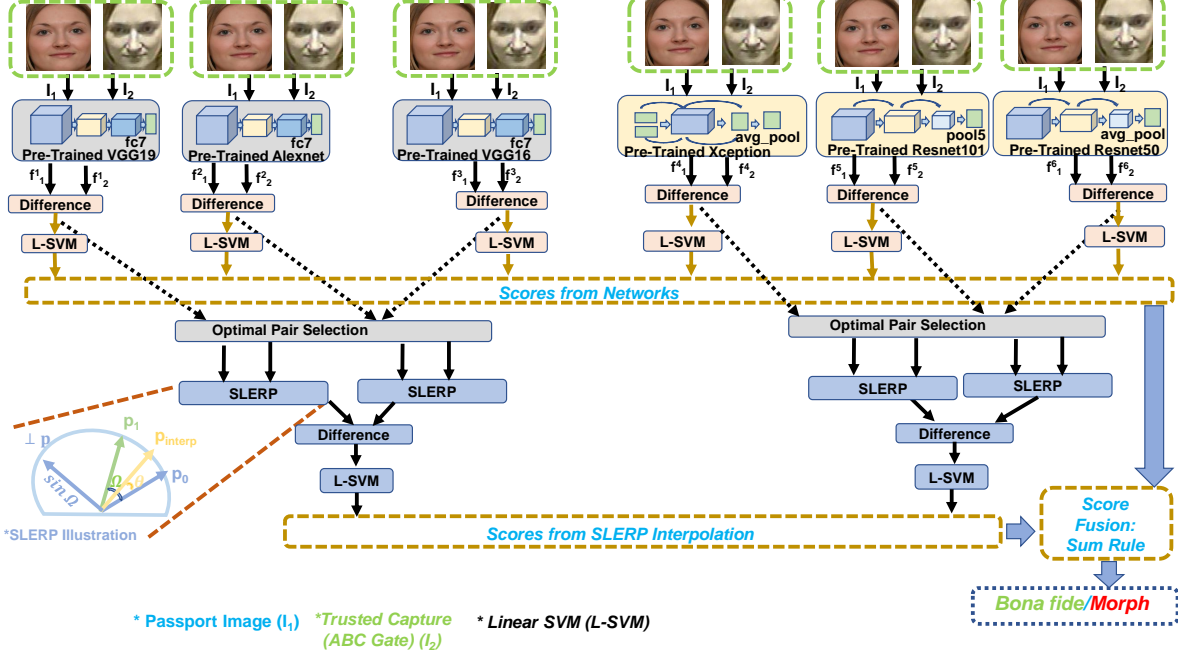


Figure 2. Illustration of the proposed Hybrid SLERP for Differential Morph Attack Detection (D-MAD).

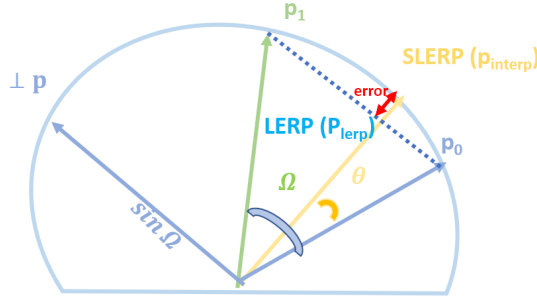


Figure 3. Illustration comparing SLERP and Linear Interpolation (LERP) where the error is highlighted in red.

generally encountered with the probe image by introducing a hierarchical fusion of deep features. The novel aspect of the proposed method is the feature interpolation fusion using Spherical Linear Interpolation (SLERP) [24] tailored to D-MAD. The proposed method will take two images I_1 and I_2 corresponding to the enrolment (from e-passport) and the trusted capture (ABC Gate) face image, respectively, to detect the morphing attack on the enrolment face image.

The primary motivation for using SLERP [24] is to perform the exact interpolation of quaternion vectors (representing a 3D rotation) on a 3D sphere. The deep features obtained for a face image are assumed to lie on a high-dimensional hypersphere [25]. Thus, linear interpolation of deep features would lie at a point on the line joining them,

but the actual interpolation should lie on the hypersphere defining the face manifold. Thus, there would be an error due to linear interpolation of deep features when compared to spherical interpolation using SLERP, which would interpolate features exactly on the hypersphere (which is also mentioned by Buss et al. [26] for 3D Sphere). This fact is illustrated in Figure 3 where the error is highlighted in red. Hence, we are motivated to use SLERP to interpolate deep features obtained corresponding to the face image. Owing to the availability of the small size face morphing datasets, the proposed method is designed using pre-trained deep CNN networks. Hence, we propose a hierarchical fusion framework to capture complementary information from different deep features effectively. The proposed D-MAD method can be structured in two functional blocks: (a) Deep feature extraction and (b) Hierarchical fusion.

2.1. Deep feature extraction

In this work, we have employed six different pre-trained deep networks trained on the ImageNet dataset [27]. The selected networks includes Alexnet [28], Resnet 50 [29], Resnet 101 [29], Xception [30], and VGG16 [31] and VGG19 [31]. These networks are selected based on their performance, and generalization for transfer learning in various applications, including morph attack detection [20]. Further, these six networks have indicated a good face morphing detection performance on various face morphing datasets [32]. Since the proposed Spherical Linear

Algorithm 1: Proposed Method

Input: Face Images I_1 and I_2
Output: (FS (Fused-Score))

- 1: Compute the features from pre-trained networks for Image (I_1).
- 2: **for** $j \leftarrow 1$ to 6 **do**
- 3: $f_1^j \leftarrow$ feature from pre-trained network.
- 4: **end for**
- 5: Compute the features from pre-trained networks for Image (I_2).
- 6: **for** $j \leftarrow 1$ to 6 **do**
- 7: $f_2^j \leftarrow$ feature from pre-trained network.
- 8: **end for**
- 9: Assign features to Groups as follows:
- 10: $G_1 \leftarrow \{f_i^j\}$ where $i \in \{1, 2\}$ and $j \in \{1 \dots 3\}$
- 11: $G_2 \leftarrow \{f_i^j\}$ where $i \in \{1, 2\}$ and $j \in \{4 \dots 6\}$
- 12: Compute the feature difference
- 13: **for** $j \leftarrow 1$ to 6 **do**
- 14: $DF^j \leftarrow f_1^j - f_2^j$
- 15: **end for**
- 16: Train Linear-SVM using difference features and compute scores
- 17: **for** $j \leftarrow 1$ to 6 **do**
- 18: $S_j \leftarrow \text{L-SVM}(DF^j)$
- 19: **end for**
- 20: Use the pre-computed pair of optimal features (x_1, y_1) and (x_1, z_1) for G_1 and (x_2, y_2) and (x_2, z_2) for G_2 . They are computed once using Equation 1.
- 21: Compute SLERP (Equation 2.2) based scores as follows where i denotes Group Index and j denotes the pair of optimal SLERP features inside it:
- 22: **for** $i \leftarrow 1$ to 2 **do**
- 23: **for** $j \leftarrow 1$ to 2 **do**
- 24: $SRP_i^j \leftarrow \text{SLERP}(f_i^{xj}, f_i^{yj})$
- 25: **end for**
- 26: Compute difference of SLERP features as $SRP_{D_i} \leftarrow SRP_i^1 - SRP_i^2$
- 27: Compute score using $S_{i+7} \leftarrow \text{L-SVM}(SRP_{D_i})$
- 28: **end for**
- 29: Generate final score by fusion using sum-rule as $(FS = \sum_{j=1}^8 S_j)$

Operator for feature interpolation requires the features to have identical dimensions, we need to choose the feature extraction from the pre-trained layers having identical dimensions. Hence, we made two groups of pre-trained networks where the first group (G_1) consists of VGG-19 (fc7), VGG-16 (fc7), and Alexnet (fc7) such that each network in this group will result in a feature dimension of 4096. The second group (G_2) consists of Xception (average pool), Resnet101 (pool5), and Resnet50 (average pool) and each

of these networks will result in a feature dimension of 2048. Thus, given the face image I_1 and I_2 from both the passport and the trusted environment (e.g., Automatic border Control Gates (ABC)), we compute the features from all six different CNN networks independently. Let the computed feature be: $F_i = f_1^i, f_2^i, \forall i = 1, \dots, 6$. Where f_1^i indicates the features from the passport image (or enrolment) corresponding to i^{th} CNN network and f_2^i corresponds to the feature from trusted source corresponding to i^{th} CNN network.

2.2. Hierarchical fusion

In the next step, we propose the hierarchical fusion of the features extracted from six different pre-trained deep CNN networks to achieve robust face morph detection performance. The proposed fusion scheme is implemented with both score-level and feature-level fusion of the features extracted from deep CNN networks. The score fusion is designed with the conventional score level fusion in which the comparison scores obtained using Linear Support Vector Machines (L-SVM) based on the feature difference vector from six different CNN networks are combined using the sum rule. Given the face images I_1 and I_2 , let the computed features be f_1^i and $f_2^i \forall i = 1, \dots, 6$. The feature difference (or residual feature computation) is performed individually for the pre-trained network $DF^i = f_1^i - f_2^i$ that is then provided to L-SVM to compute the corresponding comparison score $S^i, \forall i = 1, \dots, 6$. The second step is designed to perform the feature level fusion using Spherical Linear Operator (SLERP) [24]. As discussed earlier in Section 2.1, the feature interpolation requires the identical dimension of features. Therefore, we have grouped six different networks into two main groups; in each group, we have three different networks. In this next step, we compute the optimal basis pairs for SLERP instead of all possible random combinations for each group. This way, our approach can reduce the computation and combine the complementary features. Further, the feature combination is based on feature correlation computed using residual features to achieve robustness and generalization. Thus, given the face image I_1 and I_2 , we compute the residual feature corresponding to G_1 which is denoted as DF^1, DF^2 and DF^3 . In the next step, we compute the optimal basis pair from the triplet that can represent the complementary information to perform the residual feature combination using the SLERP method. We derive the optimal basis by computing the minimum correlation on the non-overlapping pairs generated from the given triplet, and

this is indicated in Equation1.

$$O_p = \arg \min \left\{ \begin{array}{l} \rho(\text{DF}^1, \text{DF}^2) + \rho(\text{DF}^1, \text{DF}^3), \\ \rho(\text{DF}^2, \text{DF}^1) + \rho(\text{DF}^2, \text{DF}^3), \\ \rho(\text{DF}^3, \text{DF}^1) + \rho(\text{DF}^3, \text{DF}^2) \end{array} \right\} \quad (1)$$

where ρ indicates the correlation operation and O_p indicates the optimal pairs of features. Thus,

$$\begin{aligned} S &= \{1, 2, 3\} \\ O_p &= \{\{\text{DF}^x, \text{DF}^y\}, \{\text{DF}^x, \text{DF}^z\}\} \\ \text{s.t. } (x \in S) \wedge (y, z \in S \setminus i) \wedge (y \neq z) \end{aligned} \quad (2)$$

where, x is the index of the optimal pairs, from the triplet 1, 2, 3 of features and y and z are the indices of the remaining features. The first optimum pair be $O_p^1 = \{\text{DF}^{x1}, \text{DF}^{y1}\}$ and second optimum pair be: $O_p^2 = \{\text{DF}^{x1}, \text{DF}^{z1}\}$. In the next step, we compute the SLERP feature interpolation independently for each optimum pair $O_p^s, \forall s = 1, 2$ as follows:

$$\begin{aligned} \text{Slerp}_1(\text{DF}^{x1}, \text{DF}^{y1}, t) &= \\ \frac{\sin((1-t)\Omega)}{\sin(\Omega)} \times (\text{DF}^{x1}) &+ \\ \frac{\sin((t)\Omega)}{\sin(\Omega)} \times (\text{DF}^{y1}) \end{aligned} \quad (3)$$

where, t is the interpolation factor which is set to 0.5 as recommended in [24], and Ω is the angle between the difference features DF^{x1} and DF^{y1} and can be computed using inverse cosine on dot-product as $\Omega = \arccos \text{DF}^{x1} \cdot \text{DF}^{y1}$. We computed the SLERP interpolation with the second optimal pair O_p^2 resulting in $\text{Slerp}_2(\text{DF}^{x1}, \text{DF}^{z1}, t)$.

In the next step, we perform the difference between the computed SLERP features, which is then used to compute the comparison score S_7 using L-SVM for G_1 . The procedures mentioned above are followed with G_2 to compute the comparison score S_8 . Finally, we perform the score level fusion using the sum rule to combine the scores computed from both individual CNNs and from SLERP interpolated feature differences to obtain the final score: $FS = \sum_{i=1}^8 S_i$ to make the final decision. The Algorithm of the proposed method is presented in 1.

3. Experiments and Results

In this section, we discuss the details of the newly generated face morphing dataset based on the SCFace dataset [22], performance evaluation protocols, and quantitative performance of the proposed D-MAD method.

3.1. SCFace-Morph Dataset (SCFM)

This work introduces a new dataset reflecting the OTF ABC systems with different camera resolutions and capture distances. We have employed the SCFace dataset by considering its applicability to real-life OTF face recognition with varying resolutions of the cameras and capture distances. The SCFace database is comprised of 130 data subjects that are captured with eight different cameras and three different distances, which are denoted as Distance-1 (D1) is 4.2m, Distance-2 (D2) is 2.6m, and Distance-3 (D3) is 1.0m. Face biometrics are captured as the data subjects walk (without a stop) through cameras held still with the frontal face capture. Since each data subject walks through these cameras, the captured data will be of unconstrained conditions with varying face poses that can represent the real-life ABC scenario. To effectively utilize the SCFace dataset for the face morphing application, we carefully selected the 77 unique data subjects by considering the image quality following ICAO standards [33].

Further, to reflect the real-life scenario of e-passport and ABC gates, we have considered only five different cameras that can capture visible images and high-quality mug shots. Cam1 is of resolution 540 TVL, Cam2 is of resolution 480 TVL, Cam3 is of resolution 350 TVL, Cam4 is of resolution 460 TVL, and Cam5 is of resolution 480 TVL. Thus, the mugshot images represent the face images in the e-passport. The images captured using five cameras and three different capture distances represent the trusted capture in the D-MAD algorithm evaluation. Next, we generate the face morphing dataset, the SCFace-Morph database (SCFM), using a mugshot image from the SCFace dataset. We have selected the neutral face pose image corresponding to each data subject to perform the face morphing using the landmark-based method from [23] by considering its attack potential. Before performing the morphing, the dataset of 77 data subjects is divided into two independent sets, with 56 subjects in the training set and 21 subjects in the testing set. The face morphing dataset is generated following the guidelines presented in [34] that resulted in 92 face morphing images in the training set and 28 face morphing images in the testing set. The total number of probe image samples corresponding to the training set is 840 and the testing set is 315.

The statistics of the SCFace-Morph dataset are summarized in Table 2, which specifies the number of bona fide image samples, probe image samples for each camera and capture distance and the generated face morphing images. Figure 4 shows the example face images from SCFace-Morph database dataset. To reflect the real-life scenario of border control, we also generate the re-digitized version of both morphing and bona fide mugshot images by performing print and scan operations. We have used a Ricoh IM C6000 Color Laser multi-function printer and the scan-

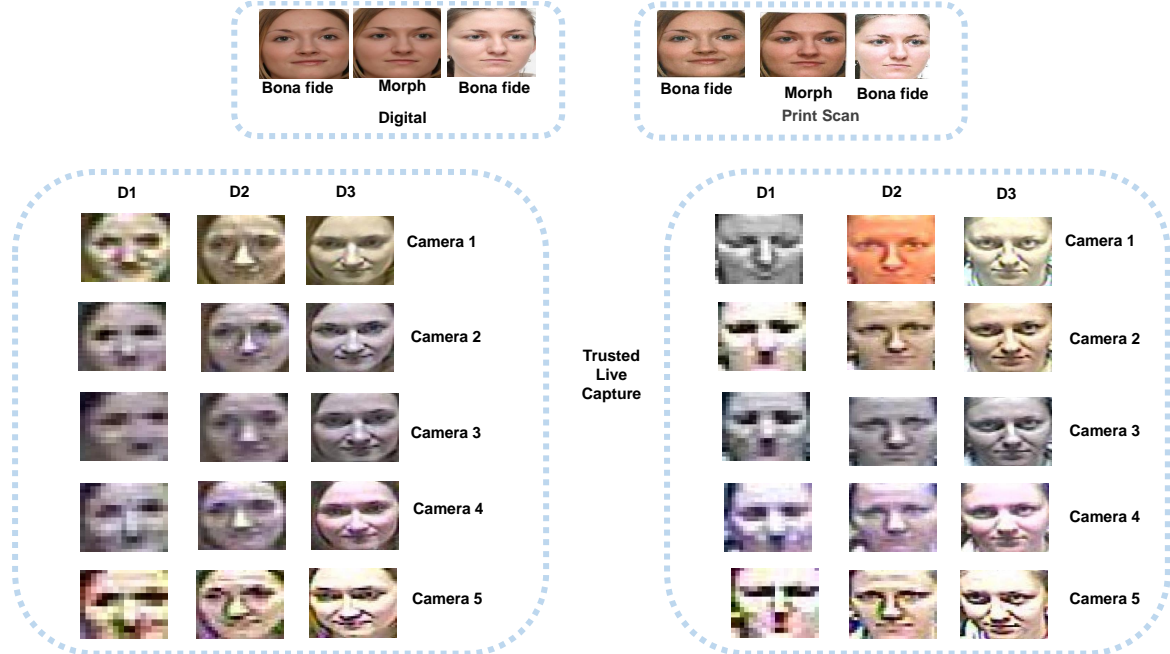


Figure 4. Example face images from SCFace-Morph Dataset (SCFM)

ner from the same printer. Facial images are scanned to have 300 dpi to match the requirement of ICAO standards [33]. Thus, the newly generated database has both digital and print-scan (PS) mediums.

3.2. Performance evaluation Protocols

We propose three performance evaluation protocols to effectively benchmark the performance of the proposed and existing D-MAD methods by considering data medium (Digital/PS), camera resolution and capture distances. **Protocol 1** is designed to analyse the performance of the D-MAD techniques with intra and inter-medium experiments independently performed on camera and capture distance. Thus, Protocol 1 will benchmark the generalisation of the D-MAD methods for the different morph data medium and their performance impact on the image resolution and capture distance. **Protocol 2** is designed to benchmark the performance of the D-MAD techniques on intra and inter-medium irrespective of the camera resolution and the capture distance. Thus, this protocol will use all camera and distance data to train and test the D-MAD methods. Hence, this protocol will indicate the generalisation performance for a different medium. **Protocol 3** is designed to benchmark the performance of the D-MAD for individual cameras and capture distance. The D-MAD algorithms are trained and tested in this protocol by merging the Digital and PS data independently for each camera and capturing distance. This protocol will reflect the real-scenario testing as all data types are used for training the D-MAD algorithm.

Hence, protocol-3 will indicate the generalisation for different camera resolutions and capture distance irrespective of data medium.

3.3. Experimental results

In this section, we present the quantitative results of the proposed method together with SOTA algorithms on D-MAD, namely Deep Feature Representation (DFR) [36] and 3D Shape and Reflectance [9]. We choose the DFR method by considering its robust performance on the NIST FRVT benchmark [37] and 3D Shape and Reflectance is selected by considering its application in the OTF ABC-based face morphing detection. The quantitative performance of the D-MAD techniques is presented using the ISO/IEC metrics [38] namely the ‘‘Attack Presentation Classification Error Rate (APCER (%))’, which defines the proportion of attack images (face morphing images) incorrectly classified as bona fide images and the Bona fide Presentation Classification Error Rate (BPCER (%)) in which bona fide images incorrectly classified as attack images are counted [38] along with the Detection Equal Error Rate (D-EER (%))’’ [39].

Table 3 indicates the quantitative performance of the D-MAD techniques on Protocol 1. Based on the obtained results, the proposed method has indicated improved results when the medium is preserved during training and testing (Intra evaluation). Further, the proposed method has indicated the best performance in the intra-evaluation protocol irrespective of the cameras and capture distances. When

Table 2. Statistics of SCFace-Morph Dataset (SCFM)

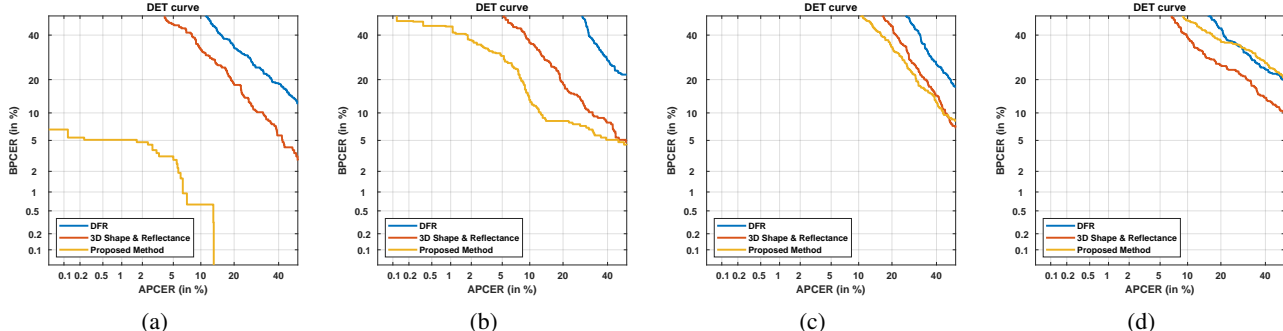


Figure 5. DET Curves for Protocol 2(a) Train: Digital and Test: Digital (b) Train: Print Scan and Test: Print Scan (c) Train: Digital and Test: Print Scan (d) Train: Print Scan and Test: Digital

Algorithm:	Distance1					Distance2					Distance3				
	Cam1	Cam2	Cam3	Cam4	Cam5	Cam1	Cam2	Cam3	Cam4	Cam5	Cam1	Cam2	Cam3	Cam4	Cam5
	D-EER (%)														
	Train: Digital, Test: Digital														
DFR [35]	23.5	23.5	28.6	20.2	23.5	28.6	28.6	28.6	24.4	28.6	33.6	24.4	28.6	28.6	23.5
3D Shape and Reflectance [9]	14.3	23.5	14.3	15.2	20.2	19.3	24.4	32.7	23.5	19.3	23.5	24.4	19.3	23.5	23.5
Proposed Method	0.9	5.1	0.0	8.3	5.1	5.2	0.9	5.1	8.3	9.2	9.2	4.2	5.1	5.1	9.2
	Train: Print Scan, Test: Print Scan														
DFR [35]	28.6	29.5	28.6	28.6	28.6	42.9	37.8	33.6	33.6	27.7	52.1	37.8	38.7	42.0	47.9
3D Shape and Reflectance [9]	19.3	23.5	42.0	23.5	23.5	19.3	20.2	33.6	27.7	23.5	28.6	32.7	23.5	28.6	23.5
Proposed Method	10.1	14.3	15.2	14.3	9.2	18.5	18.5	14.3	19.3	15.2	19.3	14.3	13.4	19.3	19.3
	Train: Digital, Test: Print Scan														
DFR	28.6	28.6	28.6	32.7	29.5	33.6	34.5	33.6	32.7	28.6	42.9	32.7	28.6	37.8	33.6
3D Shape and Reflectance	23.5	37.8	32.7	29.5	28.6	19.3	38.7	28.6	28.6	37.8	27.7	28.6	24.4	27.7	27.7
Proposed Method	28.6	23.5	28.6	29.5	29.5	32.7	24.4	28.6	37.8	28.6	33.6	33.6	34.5	37.8	33.6
	Train: Print Scan, Test: Digital														
DFR [35]	28.6	29.5	28.6	28.6	28.6	47.0	28.6	23.5	29.5	23.5	37.8	24.4	28.6	32.7	47.0
3D Shape and Reflectance [9]	24.4	33.6	42.9	33.6	32.7	27.7	28.6	24.4	23.5	27.7	32.7	29.5	29.5	28.6	24.4
Proposed Method	32.7	23.5	37.8	33.6	33.6	33.6	37.8	33.6	37.8	37.8	42.9	33.6	33.6	34.5	23.5

Table 3. Quantitative results of proposed method and SOTA on Protocol 1

Algorithm:	Train: Digital Test: Digital		Train: Print Scan Test: Print Scan		Train: Digital Test: Print Scan		Train: Print Scan Test: Digital		
	D-EER (%)	BPCER @ APCER = 5% 10%	D-EER (%)	BPCER @ APCER = 5% 10%	D-EER (%)	BPCER @ APCER = 5% 10%	D-EER (%)	BPCER @ APCER = 5% 10%	
	DFR [35]	27.1	69.5 56.8	34.7 93.3	89.2	34.3 89.2	84.1	30.9 84.1	67.3
3D Shape and Reflectance [9]	19.4	45.4 32.7	19.4 50.2	36.2 13.3	27.6 75.2	60.6 68.3	23.8 52.1	57.5 32.4	38.7 59.4
Proposed Method	3.4	3.2 0.6	11.5 29.8	26.0 13.3					47.6

Table 4. Quantitative results of proposed method and SOTA on Protocol 2

Algorithm:	Distance1					Distance2					Distance3				
	Cam1	Cam2	Cam3	Cam4	Cam5	Cam1	Cam2	Cam3	Cam4	Cam5	Cam1	Cam2	Cam3	Cam4	Cam5
	D-EER (%)														
	Train: Digital and Print Scan														
DFR [35]	32.7	32.7	32.7	28.6	30.7	35.7	32.7	30.7	35.7	35.7	40.8	42.9	32.7	32.7	37.8
3D Shape and Reflectance [9]	23.5	35.7	24.0	26.0	26.0	28.1	26.0	24.0	24.4	29.0	24.0	28.6	21.4	21.0	21.4
Proposed Method	6.7	7.6	9.7	7.6	7.6	7.1	7.6	9.7	12.2	7.6	11.8	7.6	7.6	7.1	7.1

Table 5. Quantitative results of proposed method and SOTA on Protocol 3

the medium changes during training and testing (inter evaluation), the proposed method has indicated improved per-

formance when training is performed on Digital and testing on Print Scan. The degraded performance of the program is due to the fact that the training and testing data are not consistent.

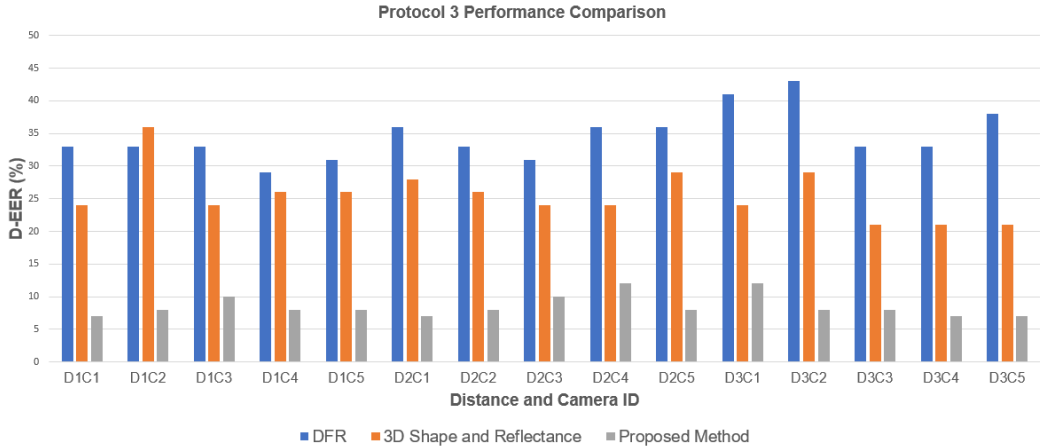


Figure 6. Illustration showing D-EER for Protocol 3 for DFR [35], 3D Shape and Reflectance [9], and Proposed Method

posed method is noted primarily in the inter-evaluation when print-scan data is used for training and digital data is used for testing. This can be attributed to the limitation of the proposed method to generalization, especially with the different image quality (because the quality of print-scan is different from that of digital) that might be due to the lack of generalized features extracted from six different pre-trained CNNs. The proposed D-MAD method generally performs better than the SOTA methods on Protocol 1.

Table 4 indicates the quantitative performance of the D-MAD techniques on Protocol 2, shown as DET curves in Figure 5. It can also be noted in this protocol that the proposed method has indicated improved performance when compared with the existing methods. The proposed method shows the best intra-evaluation protocol and comparable performance with the inter-evaluation protocol. The results indicate that the proposed method is robust to camera resolutions and capture distances.

Table 5 shows the performance of the proposed method on Protocol 3. Based on the obtained results, it can be noted that the proposed method has indicated the best performance on both cameras and different capture distances. Further, the performance of the proposed method is not influenced by the camera type and capture distance. Figure 6 graphically illustrates the D-EER performance of the D-MAD techniques on Protocol 3.

Based on the series of experiments performed, it can be noted that the D-MAD algorithms are generally influenced by the camera resolution and the capture distance. Further, the data medium will strongly influence the performance of the D-MAD algorithms in the unconstrained ABC scenario.

4. Conclusions and Future-Work

In this paper, we have presented a novel method for robust D-MAD in the ABC gate scenario. The proposed method is based on the six different pre-trained deep CNN

combined using hierarchical fusion. The proposed method's novelty is in using spherical interpolation computed by SLERP to perform the residual feature fusion. Further, the hierarchical fusion is carried out using both score and feature level to achieve the robust D-MAD. Extensive experiments on the newly generated face morphing dataset (SCFM) based on the publicly available SCFace database. The performance of the proposed method and the existing techniques are extensively evaluated using three different protocols. The evaluation protocols benchmark the D-MAD performance on the different camera resolutions and the capture distance. The obtained results have demonstrated the improved performance of the proposed method in all three protocols. The future work includes improving the generalizability of the proposed method across different morphing image qualities especially with the different print quality.

References

- [1] N. Damer, V. Boller, Y. Wainakh, F. Boutros, P. Terhorst, A. Braun, and A. Kuijper. Detecting face morphing attacks by analyzing the directed distances of facial landmarks shifts. In *Proc. of the German Conference on Pattern Recognition (GCPR)*, October 2018.
- [2] U. Scherhag, C. Rathgeb, and C. Busch. Towards detection of morphed face images in electronic travel documents. *2018 13th IAPR International Workshop on Document Analysis Systems (DAS)*, pages 187–192, April 2018. doi: 10.1109/DAS.2018.11. URL doi.ieeecomputersociety.org/10.1109/DAS.2018.11.
- [3] Naser Damer, Steffen Zienert, Yaza Wainakh, Alexandra Moseguí Saladié, Florian Kirchbuchner, and Arjan Kuijper. A multi-detector solution towards an accurate and generalized detection of face morphing attacks.

In 2019 22th International Conference on Information Fusion (FUSION), pages 1–8, 2019.

- [4] Fei Peng, Le-Bing Zhang, and Min Long. Fd-gan: Face de-morphing generative adversarial network for restoring accomplice’s facial image. *IEEE Access*, 7: 75122–75131, 2019.
- [5] Clemens Seibold, Wojciech Samek, Anna Hilsmann, and Peter Eisert. Accurate and robust neural networks for face morphing attack detection. *Journal of Information Security and Applications*, 53:102526, 2020.
- [6] Sobhan Soleymani, Baaria Chaudhary, Ali Dabouei, Jeremy Dawson, and Nasser M Nasrabadi. Differential morphed face detection using deep siamese networks. In *International Conference on Pattern Recognition*, pages 560–572. Springer, 2021.
- [7] Sobhan Soleymani, Ali Dabouei, Fariborz Taherkhani, Jeremy Dawson, and Nasser M. Nasrabadi. Mutual information maximization on disentangled representations for differential morph detection. In *Proceedings of the IEEE/CVF Winter Conference on Applications of Computer Vision (WACV)*, pages 1731–1741, January 2021.
- [8] Matteo Ferrara, Annalisa Franco, and Davide Maltoni. Face demorphing. *IEEE Transactions on Information Forensics and Security*, 13(4):1008–1017, 2017.
- [9] Jag Mohan Singh, Raghavendra Ramachandra, Kiran B Raja, and Christoph Busch. Robust morph-detection at automated border control gate using deep decomposed 3d shape & diffuse reflectance. In *2019 15th International Conference on Signal-Image Technology & Internet-Based Systems (SITIS)*, pages 106–112. IEEE, 2019.
- [10] Ulrich Scherhag, Christian Rathgeb, Johannes Merkle, and Christoph Busch. Deep face representations for differential morphing attack detection. *IEEE Transactions on Information Forensics and Security*, 15:3625–3639, 2020.
- [11] David Ortega-Delcampo, Cristina Conde, Daniel Palacios-Alonso, and Enrique Cabello. Border control morphing attack detection with a convolutional neural network de-morphing approach. *IEEE Access*, 8:92301–92313, 2020. doi: 10.1109/ACCESS.2020.2994112.
- [12] Baaria Chaudhary, Poorya Aghdaie, Sobhan Soleymani, Jeremy Dawson, and Nasser M. Nasrabadi. Differential morph face detection using discriminative wavelet sub-bands. In *Proceedings of the IEEE/CVF Conference on Computer Vision and Pattern Recognition (CVPR) Workshops*, pages 1425–1434, June 2021.
- [13] Guido Borghi, Emanuele Pancisi, Matteo Ferrara, and Davide Maltoni. A double siamese framework for differential morphing attack detection. *Sensors*, 21(10), 2021. ISSN 1424-8220. doi: 10.3390/s21103466. URL <https://www.mdpi.com/1424-8220/21/10/3466>.
- [14] Sudipta Banerjee and Arun Ross. Conditional identity disentanglement for differential face morph detection. In *2021 IEEE International Joint Conference on Biometrics (IJCB)*, pages 1–8, 2021. doi: 10.1109/IJCB52358.2021.9484355.
- [15] Ilias Batskos, Florens F de Wit, Luuk J Spreeuwers, and Raymond J Veldhuis. Preventing face morphing attacks by using legacy face images. *IET biometrics*, 10(4), 2021.
- [16] Florian Schroff, Dmitry Kalenichenko, and James Philbin. Facenet: A unified embedding for face recognition and clustering. In *Proceedings of the IEEE conference on computer vision and pattern recognition*, pages 815–823, 2015.
- [17] Omkar M. Parkhi, Andrea Vedaldi, and Andrew Zisserman. Deep face recognition. In *Proceedings of the British Machine Vision Conference (BMVC)*, pages 41.1–41.12. BMVA Press, September 2015. ISBN 1-901725-53-7. doi: 10.5244/C.29.41. URL <https://dx.doi.org/10.5244/C.29.41>.
- [18] Jiankang Deng, Jia Guo, Niannan Xue, and Stefanos Zafeiriou. Arcface: Additive angular margin loss for deep face recognition. In *Proceedings of the IEEE/CVF Conference on Computer Vision and Pattern Recognition*, pages 4690–4699, 2019.
- [19] Sankini Rancha Godage, Frøy Løvåsda, Sushma Venkatesh, Kiran Raja, Raghavendra Ramachandra, and Christoph Busch. Analyzing human observer ability in morphing attack detection—where do we stand? *arXiv e-prints*, pages arXiv–2202, 2022.
- [20] Sushma Venkatesh, Raghavendra Ramachandra, Kiran Raja, and Christoph Busch. Face morphing attack generation & detection: A comprehensive survey. *IEEE Transactions on Technology and Society*, 2021.
- [21] Kiran Raja, Matteo Ferrara, Annalisa Franco, Luuk Spreeuwers, Ilias Batskos, Florens de Wit, Marta Gomez-Barrero, Ulrich Scherhag, Daniel Fischer, Sushma Krupa Venkatesh, et al. Morphing attack

detection-database, evaluation platform, and benchmarking. *IEEE transactions on information forensics and security*, 16:4336–4351, 2020.

[22] Mislav Grgic, Kresimir Delac, and Sonja Grgic. Seface—surveillance cameras face database. *Multimedia tools and applications*, 51(3):863–879, 2011.

[23] Matteo Ferrara, Annalisa Franco, and Davide Maltoni. Decoupling texture blending and shape warping in face morphing. In *2019 International Conference of the Biometrics Special Interest Group (BIOSIG)*, pages 1–5, 2019.

[24] Ken Shoemake. Animating rotation with quaternion curves. In *Proceedings of the 12th annual conference on Computer graphics and interactive techniques*, pages 245–254, 1985.

[25] Weiyang Liu, Yandong Wen, Zhiding Yu, Ming Li, Bhiksha Raj, and Le Song. Sphereface: Deep hypersphere embedding for face recognition. In *The IEEE Conference on Computer Vision and Pattern Recognition (CVPR)*, 2017.

[26] Samuel R. Buss and Jay P. Fillmore. Spherical averages and applications to spherical splines and interpolation. *ACM Trans. Graph.*, 20(2):95–126, apr 2001. ISSN 0730-0301. doi: 10.1145/502122.502124. URL <https://doi.org/10.1145/502122.502124>.

[27] Jia Deng, Wei Dong, Richard Socher, Li-Jia Li, Kai Li, and Li Fei-Fei. Imagenet: A large-scale hierarchical image database. In *2009 IEEE conference on computer vision and pattern recognition*, pages 248–255. Ieee, 2009.

[28] Alex Krizhevsky, Ilya Sutskever, and Geoffrey E Hinton. Imagenet classification with deep convolutional neural networks. In F. Pereira, C.J. Burges, L. Bottou, and K.Q. Weinberger, editors, *Advances in Neural Information Processing Systems*, volume 25. Curran Associates, Inc., 2012. URL <https://proceedings.neurips.cc/paper/2012/file/c399862d3b9d6b76c8436e924a68c45b-Paper.pdf>.

[29] Kaiming He, Xiangyu Zhang, Shaoqing Ren, and Jian Sun. Deep residual learning for image recognition. In *Proceedings of the IEEE conference on computer vision and pattern recognition*, pages 770–778, 2016.

[30] François Chollet. Xception: Deep learning with depthwise separable convolutions. In *Proceedings of the IEEE conference on computer vision and pattern recognition*, pages 1251–1258, 2017.

[31] Karen Simonyan and Andrew Zisserman. Very deep convolutional networks for large-scale image recognition. *arXiv preprint arXiv:1409.1556*, 2014.

[32] Sushma Venkatesh, Raghavendra Ramachandra, Kiran Raja, Luuk Spreeuwers, Raymond Veldhuis, and Christoph Busch. Detecting morphed face attacks using residual noise from deep multi-scale context aggregation network. In *2020 IEEE Winter Conference on Applications of Computer Vision (WACV)*, pages 269–278, 2020. doi: 10.1109/WACV45572.2020.9093488.

[33] Andreas Wolf. Portrait quality (reference facial images for mrtd). *Version: 0.06 ICAO, Published by authority of the Secretary General*, 2016.

[34] R. Raghavendra, Kiran B. Raja, Sushma Venkatesh, and Christoph Busch. Face morphing versus face averaging: Vulnerability and detection. In *2017 IEEE International Joint Conference on Biometrics (IJCB)*, pages 555–563, 2017. doi: 10.1109/BTAS.2017.8272742.

[35] Ulrich Scherhag, Christian Rathgeb, Johannes Merkle, and Christoph Busch. Deep face representations for differential morphing attack detection. *IEEE Transactions on Information Forensics and Security*, 15:3625–3639, 2020. doi: 10.1109/TIFS.2020.2994750.

[36] Ulrich Scherhag, Luca Debiasi, Christian Rathgeb, Christoph Busch, and Andreas Uhl. Detection of face morphing attacks based on prnu analysis. *IEEE Transactions on Biometrics, Behavior, and Identity Science*, 1(4):302–317, 2019.

[37] Mei Ngan, Patrick Grother, Kayee Hanaoka, and Jason Kuo. Face recognition vendor test (frvt) part 4: Morph - performance of automated face morph detection, 2020-03-06 2020.

[38] ISO/IEC JTC1 SC37 Biometrics. *ISO/IEC IS 30107-3. Information Technology - Biometric presentation attack detection - Part 3: Testing and Reporting*. International Organization for Standardization, 2017.

[39] Haoyu Zhang, Sushma Venkatesh, Raghavendra Ramachandra, Kiran Raja, Naser Damer, and Christoph Busch. Mipgan—generating strong and high quality morphing attacks using identity prior driven gan. *IEEE Transactions on Biometrics, Behavior, and Identity Science*, 3(3):365–383, 2021.

5. Supplement Material: Reliable Face Morphing Attack Detection in On-The-Fly Border Control Scenario with Variation in Image Resolution and Capture Distance

This supplementary material presents the additional ablation results of the proposed method. We devised two experiments such that *Experiment 1*: We report both individual and intermediate results of the proposed method. *Experiment 2*: This experiment is designed to indicate the efficacy of the proposed pair selection by performing the ablation study on the different pairs. In the following, we briefly discuss the outcome of the ablation study with both experiments.

6. Quantitative results of Experiment 1

Table 6, 7 and 8 indicates the performance of the proposed method and different components used to develop the proposed method evaluated in all three protocols respectively. It can be noted that:

- The performance of the individual network varies with the train and test data type. Typically, individual CNN networks perform better when trained and tested with the same data type.
- Fusion of individual networks indicates the improved performance over the individual CNN networks based on the proposed pair selection algorithm. This intermediate fusion result is shown as SLERP Residue 1 and SLERP Residue 2.
- The proposed method has indicated the best results compared to individual and intermediate fusion results on all three protocols.

These quantitative results indicate the improved performance of the proposed method in all three protocols.

7. Quantitative results of Experiment 2

The objective of this experiment is to justify the pair selection introduced as part of the proposed method. Since pair selection is made within the groups, we proposed the pair permutation as indicated in Table 9. Tables 10, 11 and 12 indicate the quantitative results of the proposed method with different pairs in all three protocols. It can be noted that:

- The proposed algorithm for the pair selection has indicated the improved performance over other possible pairs as indicated in the Table 10, 11 and 12.
- It can be noted that the proposed pair selection did not always show the best performance in protocol 1. How-

ever, the performance of the proposed pair is comparable. The proposed pair selection shows superior performance in average statistics, as shown in Table 10.

- The proposed pair selection indicates superior performance on protocols 2 and 3. Thus, these results indicated the efficacy of the proposed pair selection algorithm, which is an integral part of the proposed method to reduce the computation without compromising the detection performance.

Thus, experiments further justify the efficacy of the proposed method for reliable face morphing detection, especially in the mixed resolution and distance ABC scenario.

Algorithm:	Distance1					Distance2					Distance3				
	Cam1	Cam2	Cam3	Cam4	Cam5	Cam1	Cam2	Cam3	Cam4	Cam5	Cam1	Cam2	Cam3	Cam4	Cam5
	D-EER (%)														
	Train: Digital, Test: Digital														
Alexnet	14.3	14.3	14.3	18.5	19.3	18.5	14.3	14.3	15.2	19.3	19.3	15.2	14.3	10.1	
VGG16	52.1	33.6	33.6	33.6	42.9	28.6	33.6	33.6	42.9	47.9	33.6	42.9	42.9	37.8	
VGG19	33.6	33.6	33.6	23.5	23.5	29.5	28.6	42.9	24.4	33.6	52.1	47.9	28.6	29.5	34.5
Resnet50	14.3	18.5	15.2	14.3	14.3	20.2	19.3	23.5	23.5	14.3	9.2	14.3	9.2	19.3	23.5
Xception	9.2	9.2	9.2	13.4	9.2	9.2	9.2	8.3	9.2	13.4	15.2	9.2	10.1	9.2	9.2
Resnet101	5.1	9.2	8.3	9.2	9.2	10.1	10.1	8.3	14.3	9.2	19.3	14.3	14.3	13.4	14.3
SLERP Residue 1	19.3	18.5	15.2	23.5	19.3	27.7	19.3	19.3	19.3	27.7	23.5	33.6	24.4	28.6	
SLERP Residue 2	24.4	19.3	9.2	19.3	24.4	37.8	23.5	28.6	42	28.6	23.5	28.6	24.4	28.6	23.5
Proposed Method	0.9	5.1	0.0	8.3	5.1	5.2	0.9	5.1	8.3	9.2	9.2	4.2	5.1	5.1	9.2
Train: Print Scan, Test: Print Scan															
Alexnet	23.5	15.2	15.2	23.5	19.3	24.4	20.2	28.6	23.5	23.5	24.4	23.5	24.4	20.2	23.5
VGG16	38.7	28.6	34.5	33.6	33.6	32.7	37.8	37.8	33.6	47.9	37.8	38.7	37.8	27.7	
VGG19	42	28.6	29.5	23.5	24.4	23.5	42.9	28.6	23.5	37.8	42.9	33.6	25.3	42.9	29.5
Resnet50	28.6	28.6	42.9	33.6	28.6	29.5	37.8	42.9	33.6	42.9	33.6	33.6	28.6	33.6	
Xception	29.5	34.5	29.5	27.7	28.6	23.5	28.6	33.6	38.7	28.6	27.7	32.7	33.6	33.6	
Resnet101	19.3	23.5	24.4	23.5	23.5	18.5	28.6	23.5	28.6	23.5	28.6	23.5	28.6	33.6	
SLERP Residue 1	24.4	27.7	28.6	37.8	23.5	27.7	27.7	33.6	37.8	37.8	23.5	28.6	33.6	37.8	
SLERP Residue 2	28.6	32.7	33.6	37.8	28.6	28.6	47.9	33.6	37.8	37.8	37.8	29.5	27.7	33.6	32.7
Proposed Method	10.1	14.3	15.2	14.3	9.2	18.5	18.5	14.3	19.3	15.2	19.3	14.3	13.4	19.3	19.3
Train: Print Scan, Test: Digital															
Alexnet	28.6	27.7	23.5	28.6	23.5	23.5	23.5	32.7	33.6	32.7	23.5	33.6	33.6	37.8	33.6
VGG16	38.7	37.8	28.6	28.6	37.8	28.6	37.8	33.6	32.7	33.6	38.7	33.6	37.8	33.6	37.8
VGG19	42	38.7	38.7	43.8	37.8	32.7	37.8	42.9	33.6	33.6	47.9	37.8	38.7	33.6	37.8
Resnet50	43.8	34.5	47.9	47.9	42.9	37.8	47.9	52.1	47	37.8	37.8	48.8	42.9	37.8	
Xception	53	47.9	52.1	47.9	52.1	52.1	57.1	57.1	47.9	57.1	47.9	47.9	52.1	57.1	48.8
Resnet101	42.9	52.1	47.9	47	47.9	52.1	43.8	56.3	47.9	37.8	58	52.1	47.9	58	47
SLERP Residue 1	28.6	27.7	38.7	29.5	27.7	28.6	37.8	37.8	42.9	42	28.6	42.9	38.7	34.5	37.8
SLERP Residue 2	47.9	47.9	56.3	42.9	52.1	37.8	38.7	42.9	57.1	38.7	42.9	52.1	47.9	48.8	
Proposed Method	28.6	23.5	28.6	29.5	29.5	32.7	24.4	28.6	37.8	28.6	33.6	33.6	34.5	37.8	33.6
Train: Print Scan, Test: Digital															
Alexnet	37.8	33.6	28.6	33.6	33.6	33.6	28.6	28.6	33.6	37.8	33.6	28.6	37.8	28.6	28.6
VGG16	52.1	42.9	43.8	38.7	47	34.5	38.7	47.9	47.9	42.9	56.3	52.1	52.1	53	38.7
VGG19	53	34.5	47	39.6	56.3	42.9	52.1	42.9	48.8	57.1	52.1	56.3	42.9	53	33.6
Resnet50	29.5	33.6	47.9	29.5	23.5	28.6	43.8	42.9	42.9	42	34.5	29.5	37.8	34.5	33.6
Xception	42	43.8	53	33.6	37.8	33.6	37.8	47.9	57.1	34.5	42.9	37.8	37.8	37.8	
Resnet101	37.8	37.8	38.7	42.9	37.8	42	37.8	43.8	42.9	52.1	42.9	33.6	37.8	47.9	52.1
SLERP Residue 1	33.6	28.6	28.6	39.6	37.8	28.6	33.6	28.6	42	33.6	37.8	37.8	42.9	47.9	29.5
SLERP Residue 2	47.9	47.9	47.9	47.9	47	29.5	38.7	42.9	37.8	47	42.9	53	47	32.7	37.8
Proposed Method	32.7	23.5	37.8	33.6	33.6	33.6	37.8	33.6	37.8	42.9	33.6	33.6	34.5	32.5	

Table 6. Experiment1: Ablation Study Protocol 1

Medium	Alexnet	VGG19	VGG16	Resnet50	Xception	Resnet101	Residue 1	Residue 2	Proposed
Train: Digital,Test: Digital	7.3	32	38.7	12	5.8	14.9	15.5	15.2	3.4
Train: Print Scan, Test: Print Scan	20.7	28.5	34.7	26.3	27	34.6	21.6	28.2	11.5
Train: Digital, Test: Print Scan	22.5	34.3	34.7	36.8	49.5	36.8	25.7	43.3	26.0
Train: Print Scan, Test: Digital	40.6	41	40	35.2	37.5	40.3	31.2	43.8	32.4

Table 7. Experiment1: Ablation Study Protocol 2

Algorithm:	Distance1					Distance2					Distance3				
	Cam1	Cam2	Cam3	Cam4	Cam5	Cam1	Cam2	Cam3	Cam4	Cam5	Cam1	Cam2	Cam3	Cam4	Cam5
	D-EER (%)														
	Train: Digital and Print Scan														
Alexnet	39.3	39.4	35.9	39.6	36.5	38.8	36.3	40	40	39.9	41.1	37.4	40.2	39.7	36.9
VGG16	46.4	48.5	47.6	46.9	47.3	49.1	48.5	46.9	48.2	47.3	50.3	49	50.7	49.1	49.4
VGG19	43.6	42	41.4	40.5	37.4	37.8	40.5	38.1	40.8	41.7	46	45.5	40.3	42	37.4
Resnet50	45.5	42	46.6	45.5	38.4	40.3	43.9	47.9	46.3	46.3	40.8	38.5	43	37.6	42.9
Xception	40.2	45.1	48.7	38.7	41.7	39.7	47.3	48.7	47.3	41.8	40	42.4	43.2	46.6	42.3
Resnet101	41.2	42	41.4	45.1	40.9	42.4	40.6	46	47	47.8	44.9	43.3	43.9	47.2	48.1
SLERP Residue 1	21.4	21.4	21.4	21.4	21.4	19.3	21.4	21.9	21.9	21.4	18.9	21	21.4	21.4	21.4
SLERP Residue 2	14.3	14.3	16.8	18.9	16.8	18.9	17.3	14.7	16.8	21.9	18.9	18.9	18.9	14.3	11.8
Proposed Method	6.7	7.6	9.7	7.6	7.6	7.1	7.6	9.7	12.2	7.6	11.8	7.6	7.6	7.1	7.1

Table 8. Experiment 1: Ablation Study Protocol 3

Pair Description		SLERP Residue 1					SLERP Residue 2				
Proposed Method Pair		(Alexnet,VGG16), (VGG16,VGG19)					(Resnet50,Resnet101),(Resnet101,Xception)				
Pair 1		(VGG16,VGG19), (VGG19,Alexnet)					(Resnet101,Xception),(Xception,Resnet50)				
Pair 2		(VGG19,Alexnet),(Alexnet,VGG16)					(Xception,Resnet50),(Resnet50,Resnet101)				

Table 9. Description of pairs used in the proposed method and Experiment 2

Algorithm:	Distance1					Distance2					Distance3					Mean D-EER %
	Cam1	Cam2	Cam3	Cam4	Cam5	Cam1	Cam2	Cam3	Cam4	Cam5	Cam1	Cam2	Cam3	Cam4	Cam5	
	D-EER (%)															
Proposed Method	0.9	5.1	0.0	8.3	5.1	5.2	0.9	5.1	8.3	9.2	9.2	4.2	5.1	5.1	9.2	5.4
Pair 1	5.1	9.2	0.9	5.1	8.3	14.3	0	5.1	0	5.1	8.3	5.1	9.2	8.3	9.2	6.2
Pair 2	5.1	9.2	4.2	9.2	4.2	9.2	0	5.1	0	5.1	9.2	4.2	5.1	5.1	8.3	5.5
Train: Digital, Test: Digital																
Proposed Method	10.1	14.3	15.2	14.3	9.2	18.5	18.5	14.3	19.3	15.2	19.3	14.3	13.4	19.3	19.3	15.6
Pair 1	15.2	14.3	23.5	19.3	9.2	14.3	20.2	19.3	27.7	15.2	20.2	10.1	19.3	19.3	19.3	17.8
Pair 2	13.4	15.2	23.5	19.3	13.4	13.4	19.3	19.3	23.5	14.3	18.5	15.2	15.2	23.5	15.2	17.5
Train: Print Scan, Test: Print Scan																
Proposed Method	28.6	23.5	28.6	29.5	29.5	32.7	24.4	28.6	37.8	28.6	33.6	33.6	34.5	37.8	33.6	31.0
Pair 1	23.5	28.6	33.6	42.9	27.7	28.6	32.7	33.6	28.6	24.4	33.6	34.5	37.8	37.8	32.7	32.0
Pair 2	24.4	27.7	33.6	28.6	27.7	24.4	29.5	38.7	34.5	23.5	37.8	37.8	38.7	42.9	33.6	32.2
Train: Print Scan, Test: Print Scan																
Proposed Method	32.7	23.5	37.8	33.6	33.6	33.6	37.8	33.6	37.8	37.8	42.9	33.6	33.6	34.5	23.5	34.0
Pair 1	37.8	33.6	42.9	28.6	29.5	33.6	37.8	33.6	42.9	34.5	42.9	33.6	38.7	42.9	33.6	36.4
Pair 2	33.6	29.5	42.9	37.8	23.5	29.5	37.8	37.8	47	37.8	47	33.6	37.8	42.9	27.7	36.4

Table 10. Experiment2: Protocol 1 Ablation Study with Pair 1 and Pair 2 whose description is provided in Table 9

D-EER (%)				
Medium		Proposed Method	Pair 1	Pair2
Train: Digital,Test: Digital		3.4	5	3.4
Train: Print Scan, Test: Print Scan		11.5	14.6	13.4
Train: Digital, Test: Print Scan		26.0	28.5	28.2
Train: Print Scan, Test: Digital		32.4	37.8	33.7

Table 11. Experiment2: Protocol 2 Ablation Study with Pair 1 and Pair 2 whose description is provided in Table 9

Algorithm:	Distance1					Distance2					Distance3					Mean D-EER %
	Cam1	Cam2	Cam3	Cam4	Cam5	Cam1	Cam2	Cam3	Cam4	Cam5	Cam1	Cam2	Cam3	Cam4	Cam5	
	D-EER (%)															
Proposed Method	6.7	7.6	9.7	7.6	7.6	7.1	7.6	9.7	12.2	7.6	11.8	7.6	7.1	7.1	7.1	7.1
Pair 1	9.7	11.8	9.7	7.6	7.1	9.2	7.6	11.8	14.7	9.7	9.7	11.8	7.1	10.1	10.1	
Pair 2	9.7	11.8	11.8	11.8	7.1	9.2	7.1	10.1	13.8	7.1	9.7	10.1	7.1	9.7	10.1	
Train: Digital and Print Scan																

Table 12. Experiment2: Protocol 3 Ablation Study with Pair 1 and Pair 2 whose description is provided in Table 9